 DOI:10.30420/566414052

Failure Diagnosis and Reconfiguration Scheme for Distributed Photovoltaic Converter Array in Solar Unmanned Aerial Vehicles

Xiongsen Zhang[1], Zhengxiao Zong[2], Fuxin Liu[1], Xuling Chen[3]

[1] College of Automation Engineering, Nanjing University of Aeronautics and Astronautics, China
[2] Shanghai Institute of Space Power-Sources, China
[3] College of Mechanical & Electrical Engineering, Nanjing University of Aeronautics and Astronautics, China

Corresponding author: Xiongsen Zhang, zhangxiongsen@nuaa.edu.cn
Speaker: Xiongsen Zhang, zhangxiongsen@nuaa.edu.cn

Abstract

Solar unmanned aerial vehicles (UAV) are usually confronted with harsh operating environments, and the photovoltaic (PV) converters used to power the solar UAV become more vulnerable. Hence, the effective fault monitoring and post-failure treatment for PV converters are required. This paper presents a fault diagnosis and reconfiguration scheme for distributed PV converter array consisting of synchronous rectification (SR) Boost converters, including a fault diagnosis method for switches by detecting the inductor current and the voltage across switches, and a fault reconfiguration scheme for PV converter array which uses the switches matrix to remove the fault module. The validity of the scheme is verified through experiments on the prototype of the PV converter array.

1 Introduction

Solar energy has been continuously researched and developed around the world with increasingly serious energy issues. For unmanned aerial vehicles (UAV), the use of photovoltaic energy can optimize the original fuel-based or battery-based power system and improve the ability of continuous work. PV system structures in UAV can be divided into centralized and distributed ones [1], in which, the distributed one can maintain the efficiency of tracking at the respective maximum power point, and further reduce the energy loss when the UAV encounter issues such as uneven illumination and shadow shading during flight, so the distributed structure is widely used in solar UAV.

Solar UAV are usually confronted with harsh operating environments, so the PV converters become more vulnerable. The overall system performance will significantly deteriorate after faults of the converters, so it is essential to carry out the fault diagnosis (FD) for PV converters and fault tolerance measure for the system. Statistics indicates that power semiconductor faults are the main faults of power electronic converters, accounting for 34% [2], and tracking the maximum power has extra thermal stresses on semiconductors [3], so the faults caused by switches are mainly studied in this paper.

Switch faults can be classified into short-circuit faults (SCF) and open-circuit faults (OCF). The research on diagnosing switch faults in non-isolated DC-DC converters based on characteristic signals has been mature. In [4], The measured inductor current and its corresponding predicted current are used to diagnose the switch fault. A novel Rogowski coil sensor has been used for diagnosis by measuring the inductor voltage [5]. In [6], the sign of the inductor current slope is used to detect the failure, while the voltage across the diode is employed as the detection signal in [7].

However, these diagnosis methods have shortcomings that logic hardware circuits are complicated. Meanwhile, as the operating frequency of the converter increases, the complexity of sampling and calculations also escalates. This paper proposes a simple method to detect the SCF and OCF of switches in SR Boost converters. The FD method is designed by sampling and processing the inductor current and the voltage across switches. This approach offers a simple structure that can be seamlessly integrated into the converter module. Additionally, this paper enhances the existing fault reconfiguration scheme [8] by introducing a module-level fault redundant scheme which uses the switches matrix to remove the fault module. The validity of the scheme is verified through experiments on the prototype of the PV converter array.

2 Structure of the Distributed PV Converter Array and Normal Operations

Fig. 1 shows the structure of the distributed PV converter array in UAV. The power from the PV panel is converted by multiple PV converters to the DC bus,

ISBN 978-3-8007-6414-3

 DOI:10.30420/566414052

with each converter capable of realizing its maximum power point tracking (MPPT), and DC bus is cascaded by the bidirectional converter and load converter to interface the storage devices and power the load. The SR Boost converter is employed as the PV converter due to its high efficiency and simple configuration.

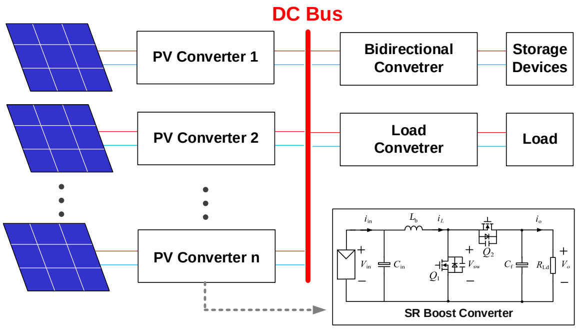

Fig. 1. Structure of the PV converter array in UAV

Fig. 2 illustrates the SR Boost converter studied in this paper, where V_{in} and V_o represent the input and output voltages. The main switch, SR switch, boost inductor, input filter capacitor and output filter capacitor are denoted by Q_1, Q_2, L_b, C_{in}, and C_f respectively. The input current, output current and inductor current are represented by i_{in}, i_o and i_L respectively. The waveforms of the converter in normal operation are shown in Fig. 3. Where D and T_s are the duty cycle of the main switch Q_1 and the switching period. Neglecting device losses and voltage drops, the relationship between the input and output voltages is $V_o = V_{in} / (1\text{-}D)$.

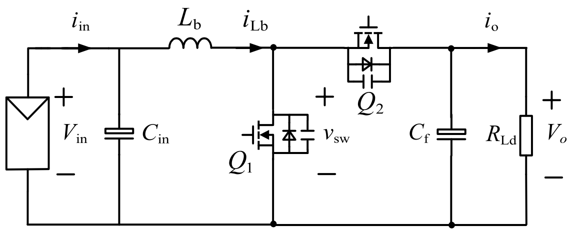

Fig. 2. Circuit topology of the SR Boost converter

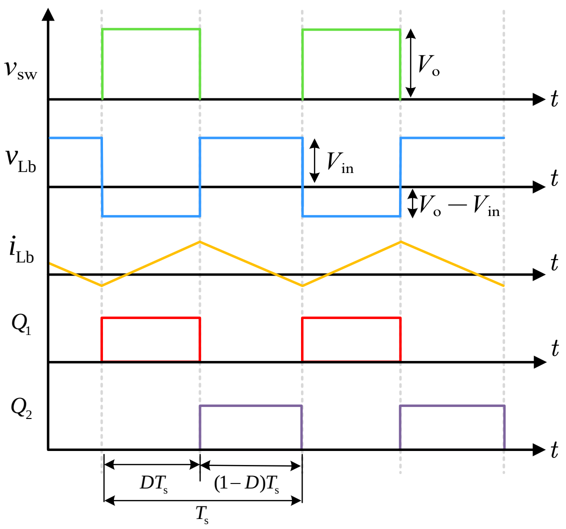

Fig. 3. Key waveforms of the SR Boost converter

3 Fault Diagnosis Method

The SR Boost converter has four typical fault conditions, i.e., SCF and OCF of main switch Q_1, SCF and OCF of SR switch Q_2. Obviously, when the switches operate in fault conditions, the current flowing through inductor and switches, and the voltage across switches will behave abnormally, thus it is possible to realize fault diagnosis by the current or voltage. In the following, the key electrical quantities will be analyzed and used for the fault diagnosis by building the equivalent model of the converter under the fault conditions mentioned above.

3.1 Q1 SCF Occurrence

Fig. 4 shows the equivalent operation modes of the SR Boost converter under Q_1 SCF. From Kirchhoff's voltage and current laws, the differential equations of the circuit in Fig. 4(a) can be formulated by

$$V_{in} = L_b \frac{di_{Lb}}{dt} + i_{Lb} r_s \tag{1}$$

where, r_s is the equivalent resistance of Q_1 under SCF.

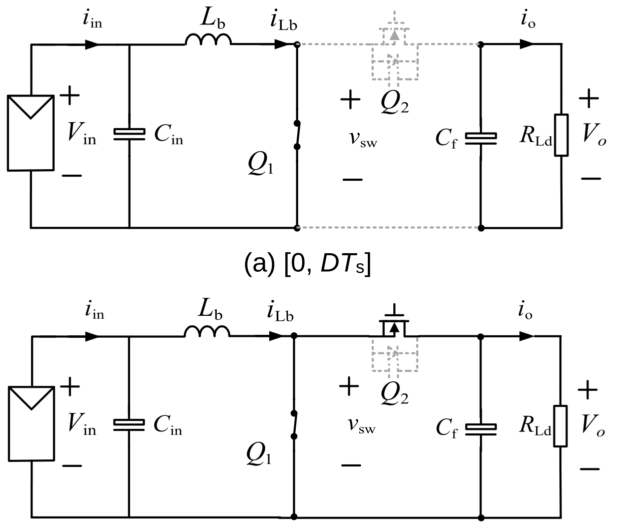

(a) [0, DT_s]

(b) [DT_s, T_s]

Fig. 4. Equivalent operation modes under Q_1 SCF

The initial conditions of the differential equations are related to the moment of fault occurrence and should have an initial value range solution for i_L,

$$\frac{V_{in}}{(1-D)^2 R_{Ld}} - \frac{V_{in}}{2L_b} DT_s \le i_{Lb}(0) \le \frac{V_{in}}{(1-D)^2 R_{Ld}} + \frac{V_{in}}{2L_b} DT_s \tag{2}$$

Neglecting the effect of inductor current ripple on the initial value of inductor current, the initial inductor current can be simplified as

$$i_{Lb}(0) \approx \frac{V_{in}}{(1-D)^2 R_{Ld}} \tag{3}$$

The inductor current is calculated by (1) and (3),

ISBN 978-3-8007-6414-3

 DOI:10.30420/566414052

$$i_{\mathrm{Lb}}(t) \approx \frac{V_{\mathrm{in}}}{r_{\mathrm{s}}} + \left[\frac{V_{\mathrm{in}}}{(1-D)^2 R_{\mathrm{Ld}}} - \frac{V_{\mathrm{in}}}{r_{\mathrm{s}}} \right] e^{-\frac{r_{\mathrm{s}}}{L_{\mathrm{b}}} t} \tag{4}$$

Since r_s is in the milliohm range, i_{Lb} rises as t increases. During [DT_s, T_s], as shown in Fig. 4(b), r_s connected with the load in parallel is still in milliohm range. The inductor is charged continuously by the input voltage and i_{Lb} will rise throughout the switching period. Therefore, Q_1 SCF can be detected by setting the upper limit of the current threshold I_{th1}, i.e., Q_1 SCF is diagnosed if $i_{Lb} > I_{th1}$. Consideration needs to be given that noises and oscillations will not falsely trigger the FD and the setting threshold should ensure the rapid response after the fault. In this paper, for the reliability of the approach, I_{th1} = 5 I_{Lb}, I_{Lb} represents the average value of the rated inductor current.

3.2 Q1 OCF Occurrence

Fig. 5 shows the equivalent modes of the SR Boost converter under Q_1 OCF. At the moment of failure, the voltage on the output filter capacitor v_{Cf} is equal to the rated output voltage V_o, and V_o is larger than the input voltage V_{in}. During [0, DT_s], as shown in Fig. 5(a), Q_2 turns off and Q_1 OCF. During [DT_s, T_s], as shown in Fig. 5(b), C_f is discharged, the output voltage gradually reduces from V_o. Eventually the converter reaches a steady state, the input voltage is applied to the load through Q_2 and its anti-parallel diode which leads to $V_{in} \approx V_o$ in this state. Neglecting converter losses, the input power $P_{in} = P_o$ and it can be deduced that $I_{in} \approx I_o$, i.e., the output current I_o will decrease and finally approach the input current I_{in} after Q_1 OCF. Comparing i_{in} and i_o through software algorithms, then the fault can be diagnosised when the difference between i_{in} and i_o is less than the threshold value I_{th2}, i.e., Q_1 OCF is diagnosed if $i_{in} - i_o < I_{th2}$.

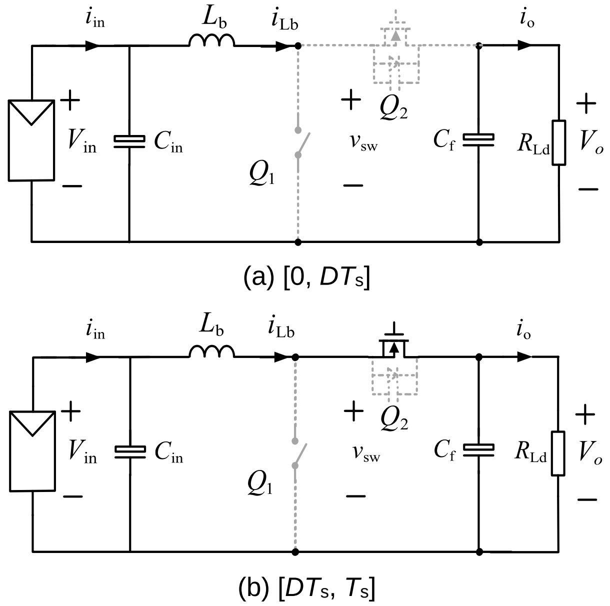

(a) [0, DT_s]

(b) [DT_s, T_s]

Fig. 5. Equivalent operation modes under Q_1 OCF

3.3 Q2 SCF Occurrence

The equivalent operation modes of the SR Boost converter under Q_2 SCF is shown in Fig. 6. During [0, DT_s], as shown in Fig. 6(a), Q_1 turns on, the input voltage is applied to L_b, and L_b stores energy. Since Q_2 SCF, C_f forms a short-circuit loop by Q_1 and Q_2. During [DT_s, T_s], as shown in Fig. 6(b), Q_1 turns off, the load is supplied by the input voltage source and L_b simultaneously and C_f is charged. Due to the equivalent resistance of Q_2 and the on-state resistance of Q_1 are in the milliohm range, the energy of C_f is mainly consumed by its equivalent series resistance (ESR). Neglecting the converter losses, the input power should be equal to the sum of the output power and the short-circuit power consumption,

$$V_{\mathrm{in}} I_{\mathrm{in}} = V_{\mathrm{o}} I_{\mathrm{o}} (1-D) + \frac{V_{\mathrm{o}}^2}{\mathrm{ESR}} D \tag{5}$$

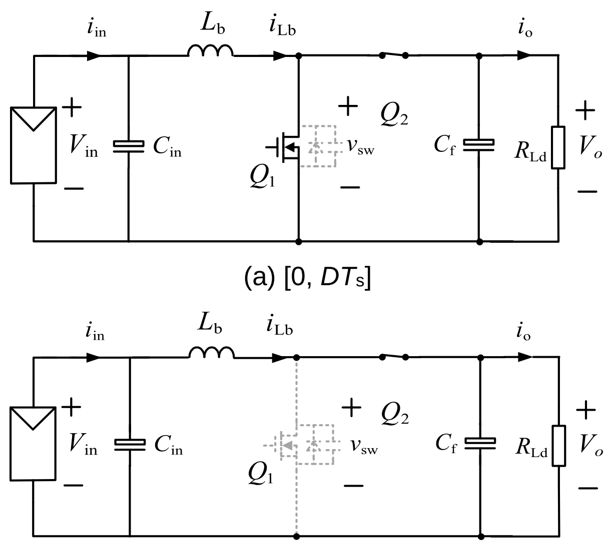

(a) [0, DT_s]

(b) [DT_s, T_s]

Fig. 6. Equivalent operation modes under Q_2 SCF

Simplifying (5), I_{in} will be

$$I_{\mathrm{in}} = \frac{V_{\mathrm{in}}}{(1-D)^2 \dfrac{R_{\mathrm{Ld}}}{1 + D\dfrac{R_{\mathrm{Ld}} - \mathrm{ESR}}{\mathrm{ESR}}}} \gg I_{\mathrm{in0}} = \frac{V_{\mathrm{in}}}{(1-D)^2 R_{\mathrm{Ld}}} \tag{6}$$

where, I_{in0} indicates the input current under normal operation.

Since $R_{Ld} \gg$ ESR, it can be concluded that $I_{in} \gg I_{in0}$ after Q_2 SCF, the input current rises continuously from the rated value. Since the input current of the converter is equal to the boost inductor current, i_{Lb} can be sampled and a upper threshold I_{th3} for comparison can be set. Q_2 SCF can be diagnosed if $i_{Lb} > I_{th3}$.

Since all FD strategies share the same remedial actions, Q_1 SCF and Q_2 SCF can be treated as one SCF. The logic hardware circuits in the system can be further simplified without affecting the FR scheme.

ISBN 978-3-8007-6414-3

 DOI:10.30420/566414052

3.4 Q2 OCF Occurrence

Fig. 7 shows the equivalent operation modes of the converter under Q_2 OCF. r_o denoted as the equivalent resistance of Q_2 under OCF condition is in the megaohm range. Due to Q_2 OCF and Q_1 turns off, i_{Lb} is approximately 0 at the initial moment.

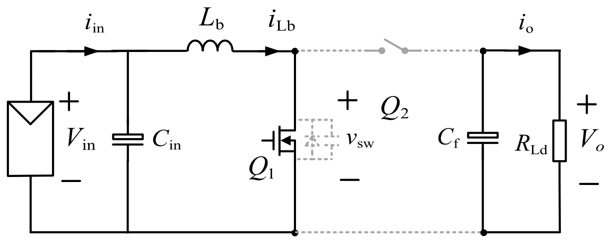

(a) [0, DT_s]

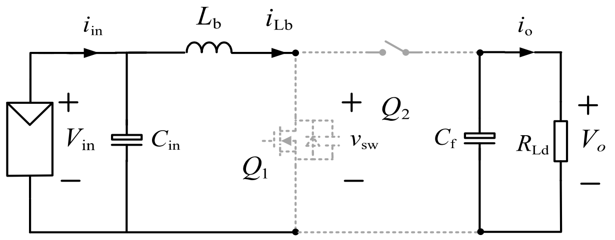

(b) [DT_s, T_s]

Fig. 7. Equivalent operation modes under Q_2 OCF

Upon entering [0, DT_s], as shown in Fig. 7(a), the input voltage is applied to the boost inductor,

$$L_b \frac{di_{Lb}}{dt} = V_{in} \tag{9}$$

During [DT_s, T_s], as shown in Fig. 7(b), Q_1 turns off and L_b forms a loop with the input voltage source, r_o and R_{Ld} to release energy, the differential equation for i_{Lb} is derived as follows:

$$\frac{di_{Lb}}{dt} = -\frac{r_o + R_{Ld}}{L_b} i_{Lb} + \frac{V_{in}}{L_b} \tag{10}$$

The initial condition is:

$$i_{Lb}(0) = \frac{V_{in}}{L_b} DT_s \tag{11}$$

As a result, the inductor voltage v_{Lb} is

$$v_{Lb}(t) = \left(V_{in} - \frac{r_o V_{in}}{L_b} DT_s \right) e^{-\frac{r_o}{L_b} t} \tag{12}$$

From (12), it can be seen that due to the large resistance value of r_o, a large voltage is generated across L_b at the moment DT_s, Furthermore, the voltage across the main switch v_{sw} could be expressed as

$$v_{sw} = V_{in} - v_{Lb} \tag{13}$$

It can be inferred that v_{sw} will experience a significant increase after Q_2 OCF. Therefore, the sampling of v_{sw} can be performed. The threshold voltage can be set as V_{th} = 1.5 V_o, and Q_2 OCF can be detected if $v_{sw} > V_{th}$.

4 Fault Reconfiguration Scheme

4.1 System Structure

When the fault in one converter is diagnosed, this converter should be removed from the PV converter array, which means the system should have the reconfiguration ability. In this paper, a system FR for post-failure operation is proposed, which improves the existing device-level reconfiguration by utilizing the switches matrix to accomplish a module-level reconfiguration.

The framework of the proposed FR scheme is shown in Fig. 8. The PV input is linked to the PV converter module via the switches matrix, which is then connected to the DC bus. Each converter module is equipped with its fault diagnosis circuit and is implemented by Digital Signal Processor (DSP) sub-controller for closed-loop algorithmic control under normal operation and diagnostic processing under fault conditions. Each module can be connected to the main-controller through Controller Area Network (CAN).

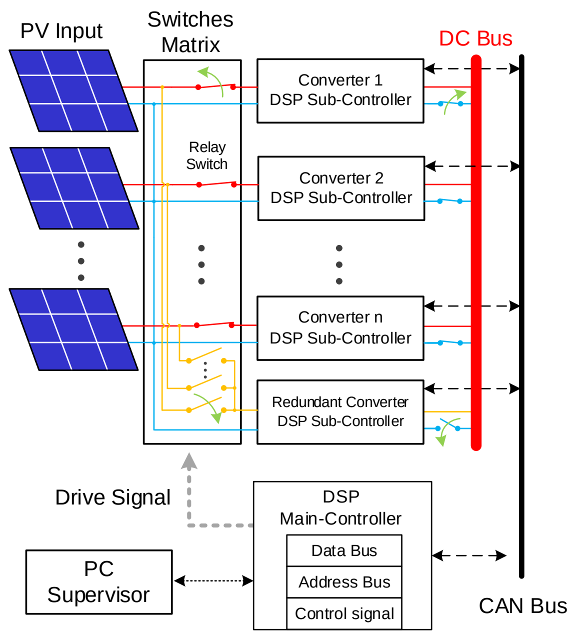

Fig. 8. FR framework of the system

This framework dedicates a system with n normal operation converter modules and one redundant converter module. The configuration can be fine-tuned to meet specific requirements, and the switches matrix for the connections should be designed accordingly.

4.2 Fault Isolation and Reconfiguration

When a fault occurs, the module promptly detects the fault using its FD method. Following fault identification, the module shuts down the driving signal forcibly and disconnects from the DC bus. Additionally, it transmits the fault information to the main-controller via CAN. The main-controller executes FR scheme, adjusts the

ISBN 978-3-8007-6414-3

 DOI:10.30420/566414052

driving signal of the switches matrix, and deactivates the relay switch corresponding to the faulty module. Concurrently, the relay switch connecting to the redundant module conducts, resuming the normal power supply of the system.

The step diagram of the FR scheme is summarized in Fig. 9. This process enables the replacement of the fault module by the redundant module.

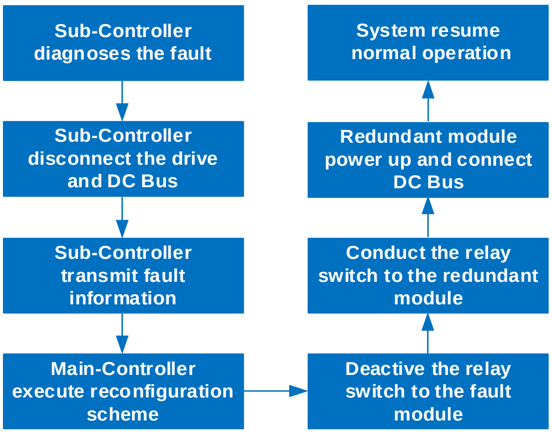

Fig. 9. Step diagram of the FR scheme

5 Experimental Results

To verify the performance of the proposed FD method and FR scheme, several experiments are carried out. The experimental setup is illustrated in Fig.10. The prototype shown in Fig.11 is simplified with one normal converter module and one redundant converter module, but the FD and FR process is same as the overall system.

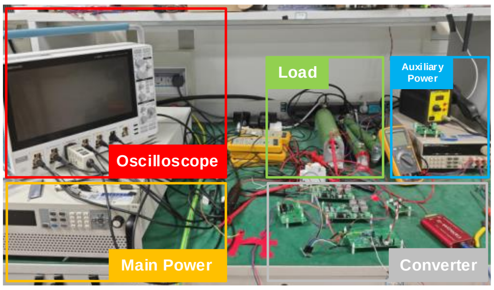

Fig. 10. Experimental setup

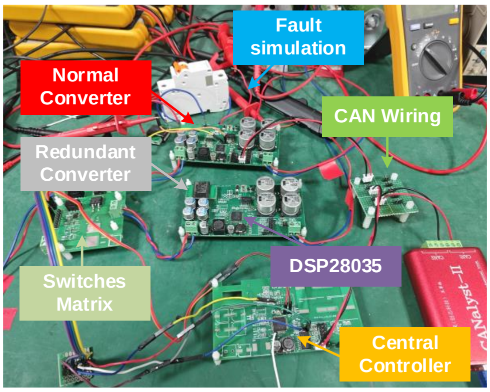

Fig. 11. Prototype of FD and FR system

All possible scenarios of converter faults including Q_1 SCF, Q_1 OCF, Q_2 SCF, Q_2 OCF are simulated with the auxiliary switch made of the circuit breaker. In the simulation of SCF, the auxiliary switch is connected in parallel with Q_1 or Q_2 and turned on for SCF. In the simulation of OCF, the auxiliary switch is connected in series with Q_1 or Q_2 and turned off for OCF. In this paper, the circuit breaker EA9AN1C16R is used as the auxiliary switch.

The specifications of the SR Boost converter are presented in Table I.

Table I

Specifications of The SR Boost Converter

Parameters	Value
V_{in}	150V
V_o	270V
Power switch	IPB60R165
L	56μH
C_{in}	20μF
C_f	100μF
R_{Ld}	243Ω
Switching frequency	150kHz

Fig.12 shows the waveforms of the SR Boost converter under normal operation, where Q_1 and Q_2 operate in a complementary manner, the maximum inductor current and maximum voltage across switches are 2 A and 270 V respectively.

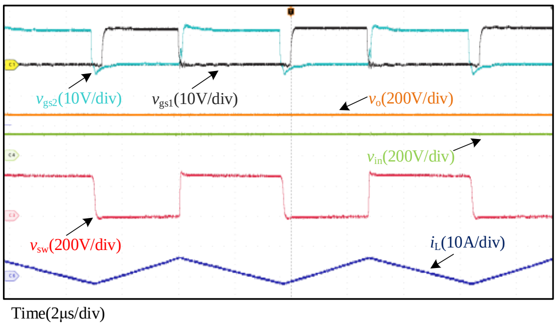

Fig. 12. Waveforms of the SR Boost converter under normal operation

Fig.13 shows the results of Q_1 SCF, where TZ_1 and TZ_2 are the diagnostic signals for Q_2 OCF and Q_1 (Q_2) SCF. When the fault occurs, the corresponding TZ signal is pulled low from 3.3V, which is sent directly to DSP for fault resnpose. A Hall sensor was used to sample i_L with the sampling value of v_{iL}. As shown, Q_1 SCF occurrs at t_1. As explained previously, i_L continues to rise to the threshold I_{th} and trigger the detection of SCF at t_2. During [t_2,t_3], the fault message is sent to main-controller and FR scheme is implemented. At t_3, the input of the redundant module rises from 0 to V_{in}, indicating the reconfiguration is accomplished, and the operation time is 255 μs.

ISBN 978-3-8007-6414-3

 DOI:10.30420/566414052

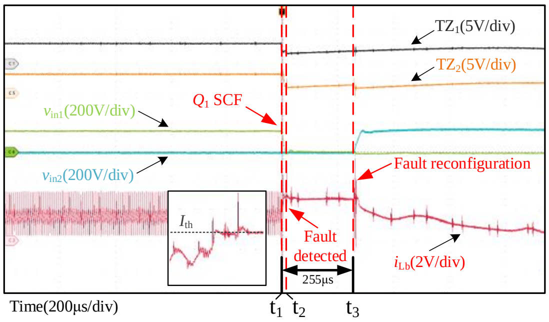

Fig. 13. Q_1 SCF detection and reconfiguration

In Fig.14, Q_1 OCF happens at t_1. Due to the use of software algorithms for fault detection, it takes more time for the controller to compute and compare, but the period [t_2,t_3] is similar to other circumstances. A total of 7471 μs have been spent for Q1 OCF detection and reconfiguration.

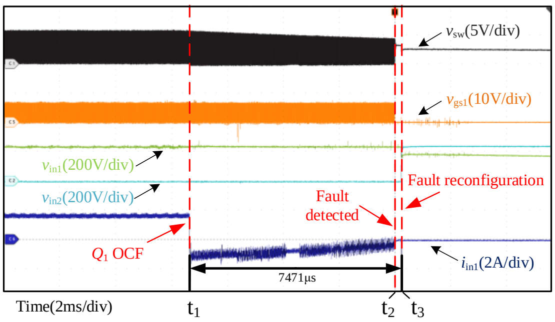

Fig. 14. Q_1 OCF detection and reconfiguration

Fig.15 dedicates the experiment of Q_2 SCF, the detection method used is the same as in Q_1 SCF . C_f first undergoes a reverse discharge process, after which i_L rises above I_{th} and triggers SCF detection.The time of fault detection and reconfiguration is 850 μs in total.

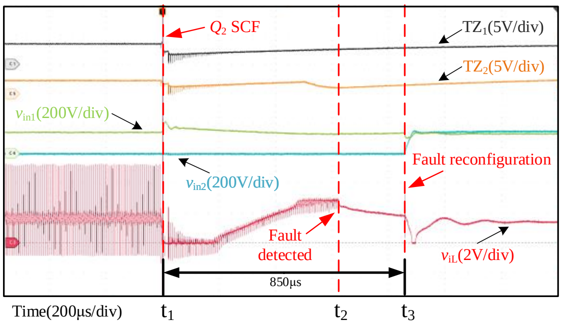

Fig. 15. Q_2 SCF detection and reconfiguration

Fig.16 shows the waveforms of Q_2 OCF, as discussed before, the inductor stores energy and releases through the switch, which leads to a large voltage rise across the main switch. The sampled v_{sw} will exceed the threshold V_{th}, causing TZ_1 signal to be pulled low and triggering Q_2 OCF at t_2. The system is reconfigured through the period [t_2,t_3], taking 398 μs to complete the operation.

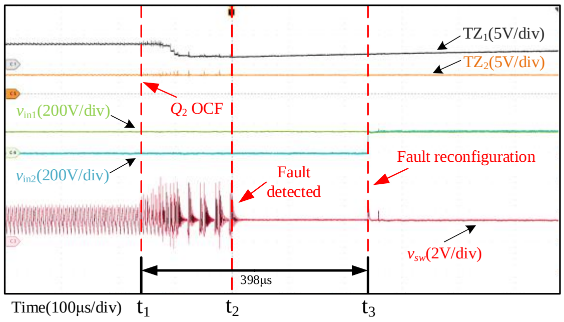

Fig. 16. Q_2 OCF detection and reconfiguration

6 Conclusion

This paper proposes a fault diagnosis method for switches in the SR Boost converter that serves as the PV converter in solar UAV by detecting the inductor current and the voltage across switches, and a fault reconfiguration scheme for distributed PV converter array which uses the switches matrix to remove the fault module. The proposed diagnosis method can detect the switch fault with a simple hardware circuit under high operating frequency. Meanwhile, the fault information can be uploaded and processed after the fault occurs. The main-controller can receive the fault information and implement the reconfiguration scheme. The fault module can be removed and the redundant module can cut in by the switches matrix. The system can resume normal operation up to 7471 μs, which was verified experimentally.

7 References

[1] M. S. Agamy et al., "An Efficient Partial Power Processing DC/DC Converter for Distributed PV Architectures," in IEEE Transactions on Power Electronics, vol. 29, no. 2, pp. 674-686, Feb. 2014.

[2] R. Wu, F. Blaabjerg, H. Wang, M. Liserre and F. Iannuzzo, "Catastrophic Failure and Fault-tolerant Design of IGBT Power Electronic Converters ," IECON 2013 - 39th Annual Conference of the IEEE Industrial Electronics Society, Vienna, Austria, 2013, pp. 507-513.

[3] Batunlu, Canras, Mohamad Alrweq and Alhussein Albarbar. “Effects of Power Tracking Algorithms on Lifetime of Power Electronic Devices Used in Solar Systems.” *Energies* 9 (2016): 1-23.

[4] E. Pazouki, Y. Sozer and J. A. De Abreu-Garcia, "Fault Diagnosis and Fault-Tolerant Control Operation of Nonisolated DC–DC Converters," in IEEE Transactions on Industry Applications, vol. 54, no. 1, pp. 310-320, Jan.-Feb. 2018.

[5] E. Farjah, H. Givi and T. Ghanbari, "Application of an Efficient Rogowski Coil Sensor for Switch Fault

Diagnosis and Capacitor ESR Monitoring in Nonisolated Single-Switch DC–DC Converters," in IEEE Transactions on Power Electronics, vol. 32, no. 2, pp. 1442-1456, Feb. 2017.

[6] E. Jamshidpour, P. Poure, E. Gholipour and S. Saadate, "Single-Switch DC–DC Converter With Fault-Tolerant Capability Under Open- and Short-Circuit Switch Failures," in IEEE Transactions on Power Electronics, vol. 30, no. 5, pp. 2703-2712, May 2015.

[7] H. Givi, E. Farjah and T. Ghanbari, "Switch and Diode Fault Diagnosis in Nonisolated DC–DC Converters Using Diode Voltage Signature," in IEEE Transactions on Industrial Electronics, vol. 65, no. 2, pp. 1606-1615, Feb. 2018.

[8] E. Jamshidpour, P. Poure and S. Saadate, "Photovoltaic Systems Reliability Improvement by Real-Time FPGA-Based Switch Failure Diagnosis and Fault-Tolerant DC–DC Converter," in IEEE Transactions on Industrial Electronics, vol. 62, no. 11, pp. 7247-7255, Nov. 2015.